Space Sci Rev (2020) 216:135
https://doi.org/10.1007/s11214-020-00766-8

The Chinese Mars ROVER Fluxgate Magnetometers

A.M. Du[1,2,3] · Y. Zhang[1,2] · H.Y. Li[4] · D.H. Qiao[5] · Z. Yi[6] · T.L. Zhang[7,8] · L.F. Meng[6] · Y.S. Ge[1,2] · H. Luo[1,2] · L. Zhao[1,2] · S.Q. Sun[1,2] · J.M. Ou[1,2,3] · Z. Li[1,2] · X. Feng[1,2] · J.L. Dai[6]

Received: 9 June 2020 / Accepted: 9 November 2020 / Published online: 20 November 2020

Abstract The Mars Rover Magnetometers (RoMAG) will implement the first mobile magnetic field measurements on the surface of Mars. Two identical tri-axial fluxgate magnetometer sensors are mounted at the top and bottom of the mast of rover, respectively. The technology of Helmholtz compensation coil probe and digital closed-loop feedback circuit is utilized to realize high precision measurement. Each magnetometer measures the vector magnetic field with a resolution of 0.01 nT in the range of ±65000 nT. The sample rate is up to 32 Hz and the noise is 0.01 nT/$\sqrt{\text{Hz}}$ @1 Hz. A rover magnetic compensation procedure was conducted to remove the most important magnetic disturbances. Mobile magnetic field measurements on the Martian surface would obtain fine-scale crust field and provide information about its remnant magnetization and any possible intrinsic magnetic field. It would help us to further understand Martian internal structure, coupling processes of solar wind-magnetosphere-ionosphere.

Keywords Mars · Magnetic field · Magnetometer · Rover · Calibration

The Huoxing-1 (HX-1) / Tianwen-1 (TW-1) mission to Mars
Edited by Chunlai Li and Jianjun Liu

✉ Y. Zhang
yzhang@mail.iggcas.ac.cn

1 Key Laboratory of Earth and Planetary Physics, Institute of Geology and Geophysics, Chinese Academy of Sciences, Beijing, 100029, China

2 College of Earth Science, University of Chinese Academy of Sciences, Beijing, China

3 State Key Laboratory of Lunar and Planetary Sciences, Macau University of Science and Technology, Macau, China

4 National Astronomical Observatories, Chinese Academy of Sciences, Beijing, 100101, China

5 School of Electronic and Information Engineering, Soochow University, Soochow, China

6 Beijing Institute of Spacecraft Environment Engineering, Beijing, 100094, China

7 CAS Center for Excellence in Comparative Planetology, Hefei, 230026, China

8 Space Research Institute, Austrian Academy of Sciences, Graz, Austria

Table 1 The missions of Martian magnetic field measurement

No.	Mission	Country/region	Launch time	Instrument	Sampling rates	Range/resolution	Installation location
1	Mariner 4	USA	1964	Helium vector magnetometer	0.9 s; 1.5 s; 2.4 s	±320 nT/0.35 nT	On a boom
2	Mars 2	USSR	1971	Triaxial fluxgate magnetometer	1 min	±60 nT/1 nT	On a boom
3	Mars 3	USSR	1971	Triaxial fluxgate magnetometer	1 min	±60 nT/1 nT	On a boom
4	Mars 5	USSR	1973	Triaxial fluxgate magnetometer	1 min	±60 nT/1 nT	On a boom
5	Phobos 2	USSR	1988	Two Triaxial fluxgate magnetometer	1.5 s; 2.4 s; 40 s; 600 s;	±100 nT/0.05 nT	At the end of Solar array
6	MGS	USA	1996	Two Triaxial fluxgate magnetometer	1/8 s; 1/16 s; 1/32 s	±4 nT/0.002 nT ±16 nT/0.008 nT ±64 nT/0.032 nT ±256 nT/0.128 nT ±1024 nT/0.512 nT ±4096 nT/2.048 nT ±16384 nT/8.192 nT ±65536 nT/32.768 nT	At the tips of Surveyor's two solar panels
7	Rosetta	ESA	2004	Two Triaxial fluxgate magnetometer	0.05 s	±16384 nT/0.031 nT	On a boom
8	Maven	USA	2013	Two Triaxial fluxgate magnetometer	1/32 s	±512 nT/0.015 nT ±2048 nT/0.062 nT ±65536 nT/2 nT	At the outer extremity of the two solar arrays on small extensions
9	Insight	USA	2018	Triaxial fluxgate magnetometer	1/20 s	±20000 nT/0.01 nT	On the deck of the Lander
10	TianWen-1	CHN	2020	Two Triaxial fluxgate magnetometer	1/32 s	±65000 nT/0.01 nT	On the mast of Rover

1 Introduction

Martian magnetic field plays an important role in investigating the Martian interior structure and evolution, and monitoring the space environments (Johnson et al. 2020). Martian magnetometry measurements can make us to acquire important observation data to study the space distribution of Martian crust magnetic field, the origin and evolution of magnetic field, the relation to geological structure, and the interaction between solar wind and Martian ionosphere. The expected research results would help us to understand Martian internal structure, space electromagnetic environment, and the evolutionary history of atmosphere and climate.

The magnetic explorations of the Mars have been accomplished by magnetometers on the flyby spacecraft and the orbiters since 1960s. The payload information of Martian magnetic field measurement based on the effective magnetic field data is shown in Table 1 (Smith et al. 1965; Dolginov et al. 1973, 1976; Acuña et al. 1998, 1999, 2001; Auster et al. 2008; Banfield et al. 2019). Mariner 4 flew by Mars on July 15, 1965. The first magnetic measurement is

implemented at a distance of 3.9 Mars radii (Smith et al. 1965; Riedler et al. 1989). MGS produced an unprecedented global map of crust magnetic fields at around 400 km altitude (Connerney et al. 2005). MAVEN performed more complete study of the magnetic field magnitudes at a lowest target altitude of 125 km (Connerney et al. 2015). The magnetometer installed on the Insight Lander, which is launched in 2018, brought opportunities to directly measure the magnetic field on the surface of Mars. It was found that the field on the surface is ten times stronger than expected and the data implied it was coming from nearby sources (Johnson et al. 2020).

The magnetometer mounted on Insight lander gives new knowledges of the Martian surface magnetic field. However, due to the limitation of the single point measurement, the sources of some new discovering phenomena are open questions. The RoMAG payload of TianWen-1 mission will provide the first mobile magnetic field measurements on the Martian surface. High space resolution multi-point mobile measurements of RoMAG could make us to obtain the fine-scale profile of Martian crust field along the rover track, and also could investigate magnetic field distribution around a magnetic target in detail. Combining the two-site observation by RoMAG and Insight and the Obiter magnetometer observation of TianWen-1, we can add constraints in modeling the global crust magnetic field, explain the interior structure of Mars, and study the features of the Martian magnetic waves on surface. It would provide an unprecedent opportunity for Martian magnetic field investigation.

2 Science Requirements

As one of the important payloads of the Chinese Mars Rover, RoMAG will provide high space resolution magnetic measurements of surface. The major unresolved questions are: When and how did the Martian dynamo die? What cause the asymmetry in Martian crust magnetic field strengths? How does the magnetic field interact with the solar wind? The science objectives are listed as follows:

(1) To obtain fine-scale structures of crustal magnetic field based on the mobile measurements on the Martian surface.
(2) Combining with Chinese Mars Orbiter observation, to study the ionospheric conductivity by inverting the ionospheric dynamo current.
(3) To study the Martian internal structure.

RoMAG consists of two identical tri-axial fluxgates (Fig. 1). The two sensors are mounted on the top and bottom of the mast of Rover, respectively. The distance between them is 67.5 cm. Above the magnetometer sensor 1, a Multispectral Camera (MSCam) and a Navigation and Terrain Camera (NaTeCam) are mounted. Other payloads, Rover-mounted Subsurface Penetrating Radar (RoSPR), Mars Climate Station (MCS), and Mars Surface Composition Detector (MarSCoDe), are also installed on the Mars Rover. The six instruments are designed for a detailed characterization of the Martian surface. The sensor installation environments and the above-mentioned science objectives enforce some basic requirements to the magnetometers. RoMAG requirements are listed as follows:

(1) The range of magnetometer needed to exceed the sum of the Mars surface magnetic field and the Mars Rover magnetic field. Therefore, we chose a range for the magnetometer of $\pm 65{,}000$ nT.
(2) Sample rate sufficient to provide temporal resolution of 32 seconds or better.

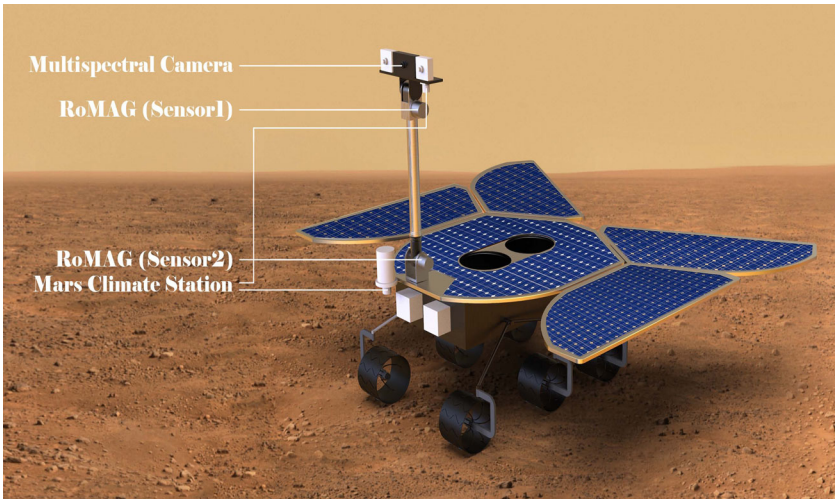

Fig. 1 The cartoon of Chinese Mars Rover. Two tri-axial magnetometers are mounted on the top and bottom of the mast of Rover, respectively

Table 2 Magnetometer sensor performance

Sensor type	Two tri-axial ring core fluxgates
Intrinsic noise level	10 pT/$\sqrt{}$Hz at 1 Hz
Ranges	±65000 nT
Digital resolution	0.01 nT
Sample rate	1/32 s; 1/16 s; 1 s
Mass	
Sensor	86 g
Electronic	628.9 g
Dimension	
Sensor	Diameter 68 mm, height 43 mm
Electronic	233 mm × 281 mm × 14 mm
Power Consumption	5.48 w

(3) The diurnal variation of the magnetic field on the surface is about 30 nT (Johnson et al. 2020). In order to trace the actual field variation of small changes, a resolution of at least 0.1 nT is required.
(4) The magnetometer noise requirement is 0.01 nT/$\sqrt{}$Hz at 1 Hz.

The performance parameters of magnetometer sensors are summarized in Table 2.

3 Instruments Description

Tri-axial ring core fluxgate sensors have been used for various space missions. The RoMAG system is designed based on the sensor system developed for THEMIS (Auster et al. 2008), VenusExpress (Zhang et al. 2006), the ROSETTA lander Philae (Auster et al. 2007), BepiColombo (Glassmeier et al. 2010), and MASCOT (Herčík et al. 2016) by the University of Braunschweig in cooperation with the MAGSON GmbH in Berlin. The sensors and

Fig. 2 The structure (left) and the packaged appearance (right) of RoMAG sensor

electronic units have been manufactured at the Institute of Geology and Geophysics (IGG), Chinese Academy of Sciences (CAS).

3.1 Principle of Operation

The three-axis fluxgate magnetometer (FGM) is a ring core system with vector-compensated consisting of sensor and digital electronics. The measurement principle of a fluxgate magnetometer is based on the high permeable soft-magnetic ring cores being driven into deep saturation by an excitation current with specific frequency. An existing external magnetic field distorts the symmetry of the magnetic flux within the core. A signal in even harmonics of the excitation frequency can be generated and it is proportional to the external field. The sense coil system is designed for the selective measurement of the excitation frequency's second harmonic. A feedback current in the enclosing Helmholtz coil system is generated to compensate the external field at the ring core position. The single component values of the external field are calculated utilizing the field-proportional feedback current values and the remaining field at the core position.

3.2 Fluxgate Sensor

The fluxgate sensor consists of excitation coils, pick-up coils, feedback coils, thermistor and skeleton. The excitation signals are driven by two crossed ring cores with a diameter of 13 and 18 mm. The excitation coils are surrounded by three pick-up coil pairs for the X, Y and Z components. A vector compensating feedback coil system is used to keep the ring cores in zero field. In order to guarantees a wide temperature range and a temperature independent axis alignment, the material of the feedback system is choosing to have a similar thermal expansion coefficient. As shown in Fig. 2, the sensor coil system is encapsulated in a cylindrical polysulfide shell and connected to the electronics via a long pigtail harness (286.4 cm for Sensor 1, 167.7 cm for Sensor 2). The two sensors with their covers and pigtails have a mass of 259.9 g and 156.5 g, respectively.

3.3 Sensor Electronics

The block diagram of the RoMAG sensor electronics is illustrated in Fig. 3. The hardware of electronics unit is composed of excitation circuitry, preamplifier, feedback current sources, high precision ADCs/DACs and temperature circuitry.

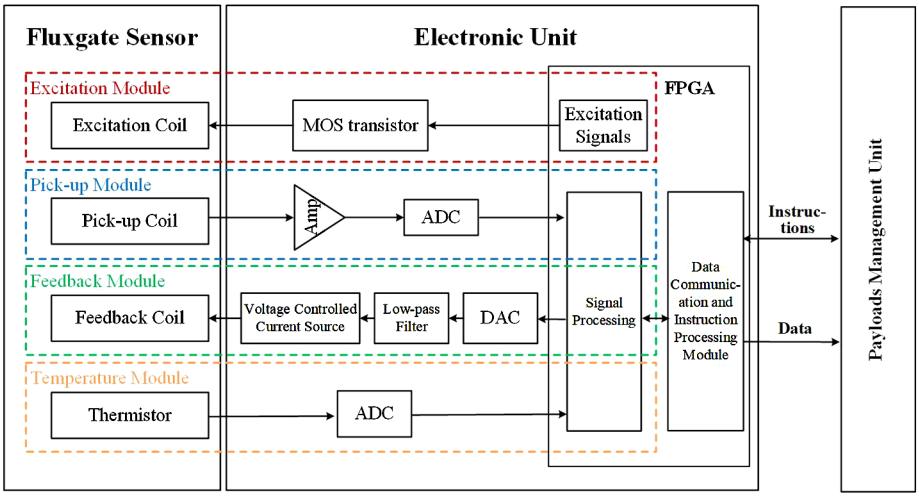

Fig. 3 Block diagram of the Digital Fluxgate

Table 3 The noise level for two magnetometers

Parameter		Sensor 1	Sensor 2
Noise (pT/$\sqrt{}$Hz @1 Hz)	X	6.2	10.0
	Y	6.0	7.8
	Z	7.8	10.0

Instrument control, digital data processing, instruction parsing and data processing are implemented in a Field-Programmable Gate Array (FPGA). The temperature circuitry is designed to collect the temperature data, which is used to calibrate thermal drift coefficients, of sensor and electronics board.

The sensor electronics generates an excitation AC current. The fundamental excitation frequency is about 9.6 kHz and the sampling rate is 80–160 kHz. The output signal from the pick-up coil is amplified and then sampled and converted by the ADC and transmitted to the FPGA. In FPGAs, fast digitization of the sensor AC-signal and the subsequent data processing are implemented. Prior to the data processing, a band-pass filtering around the second harmonics is performed to alleviate the aliasing problem. The feedback field improves the overall linearity and stability of the magnetometer. Feedback signals are produced by a set of two 12-bit digital-to-analogue converters (DACs) and a separate pair of feedback coils (Helmholtz coils) per sensor axis. The sense values from the analogue-to-digital converter (ADC) and the feedback values are continuously used for calculating the magnetic field values. Using the D/A digital compensation, the aliasing signal and bias field is gradually minimized and the dynamic compensation is then accomplished. Meanwhile, the instrument noise is then reduced. The noise level of the magnetometers is shown in Fig. 4. The noise levels at 1 Hz on the two magnetometers are shown in Table 3, which well satisfy the scientific requirement.

The instrument electronics unit is placed in the payloads management unit box together with other payload electronic boards. The electronics board uses ±12 V, ±5 V, ±3.3 V power provided by the payloads management unit and converts these voltages to those re-

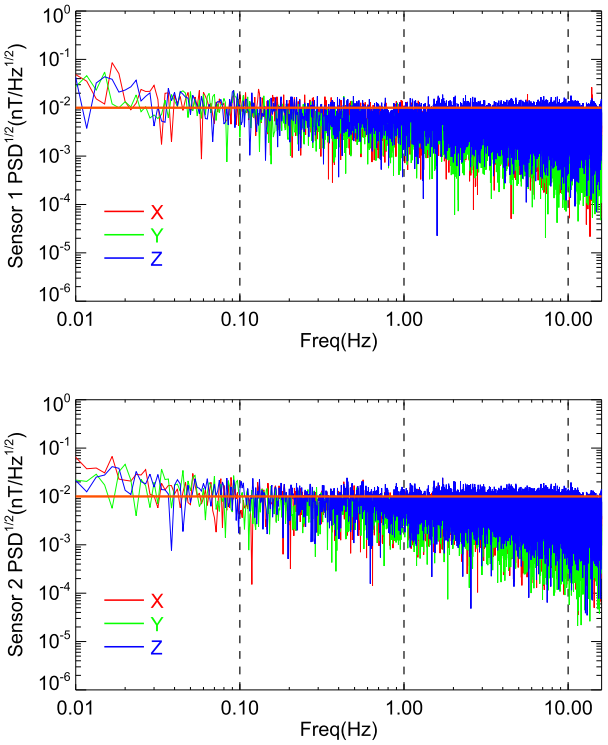

Fig. 4 Noise in each axis as a function of frequency for the two magnetometers. X-axis noise is in red, y-axis in green, and z-axis in blue. The requirement is in orange color

quired by the electronics. The electronics unit (Fig. 5) is 23.3 × 28.1 × 1.4 cm, the power consumption is 5.48 W, and its mass adds up to 628.9 g.

3.4 Ground Test and Calibration

In order to qualify the sensors for flight, the instrument space-qualification tests, such as the thermal cycle, thermal vacuum, vibration, shock, electromagnetic compatibility (EMC), have been completed in preflight. To verify the performance of the RoMAG in nominal and extreme temperature, the sensors were thermally cycled 12.5 times over the temperature range −65 °C and +60 °C.

In preflight, RoMAG was calibrated in the calibration facility of the Weak Magnetic Metering Station in the city of Yichang, Hubei Province, China. This laboratory for magnetometer calibrations located on a mountain outside the Yichang city and far away from major magnetic disturbers.

Figure 6 shows the calibrations facility with a large Helmholtz coil system. The test of the dependency of instrument parameter on temperature was also performed. The sensor and electronics boards were put inside a temperature box. The temperature has been varied between −60 °C and +60 °C. The sensor was placed in a coil system, in which the field can be changed by varying electric current. By generating test fields, the sensor offset can be checked. The RoMAG sensor was placed in a thermal box (Fig. 7), allowing the sensor to be tested at various temperatures in a range from −60 °C to +60 °C.

The calibration procedure includes the determination of the instrument performance in terms of the scale, offset, and internal misalignment. The calibration parameters are given

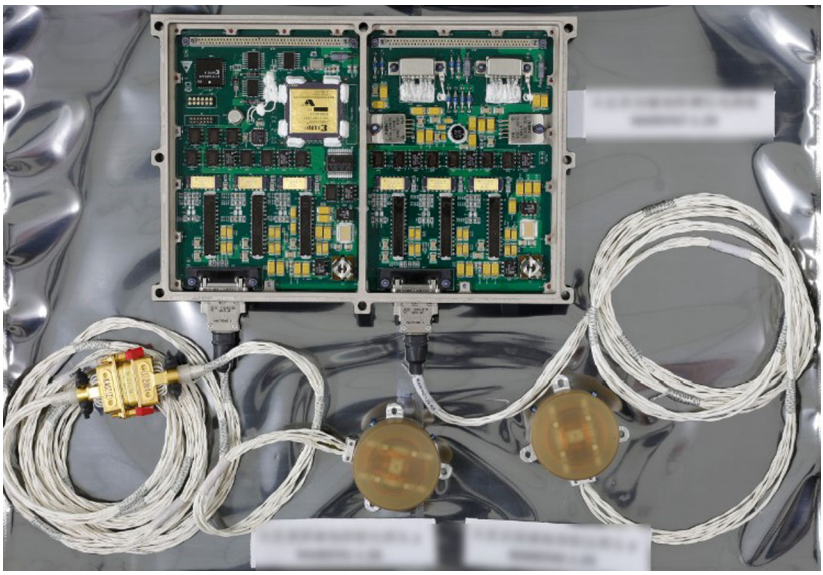

Fig. 5 The RoMAG electronics with the two sensors

Fig. 6 The Calibration Facility: a 2.4 m large Helmholtz coil system

in Table 4. The magnetometer output $\boldsymbol{B}_{fgm}$ can be expressed as a linear response of the true field vector $\boldsymbol{B}_{tr}$ (Olsen et al. 2003)

$$\boldsymbol{B}_{fgm} = \boldsymbol{S} \cdot \boldsymbol{P} \cdot \boldsymbol{B}_{tr} + \boldsymbol{O} \tag{1}$$

where $\boldsymbol{S}$ is a diagonal matrix of scale factors, $\boldsymbol{P}$ is orthogonality matrix, $\boldsymbol{O}$ is offset vector. Based on the calibration parameters, the calibrated field can be computed by applying the calibration matrix to the data measured by the magnetometer sensor after removal of the sensor offset.

3.5 Rover-Generated Field Estimation and Compensation

Due to size limitations and mass constraints, RoMAG is accommodated directly to mount on the mast of rover in the vicinity of other payloads and system sub-units. The magnetometers measure the superposition of the ambient field plus the field that produced by different

Fig. 7 The thermal box with a coil system

Table 4 The calibration parameters

Parameter		Sensor 1	Sensor 2
Scale Factor	S_x	0.857	0.847
	S_y	0.806	0.803
	S_z	0.921	0.923
Offset (nT)	O_x	−584.6	−385.7
	O_y	−350.4	−531.2
	O_z	−363.6	−586.0
Misalignment (deg)	U_{xy}	89.71	89.25
	U_{xz}	89.71	89.83
	U_{yz}	89.81	89.70

sources on the Rover. It is a challenge to accurately estimate and compensate the rover-generated magnetic field from a variety of sources.

To identify correctly what mechanism or subsystem is responsible for the interference, we conduct specialized prelaunch magnetic tests to identify the most important sources. It is found that there is a strong magnet of micro-motor in vicinity of each sensor. Additional sources are associated with the operation of other payloads. It should be noted that NaTeCam and RoSPR were advised to remain power off during the operation period of RoMAG.

In order to qualify the rover-generated interference, we implement a prelaunch magnetic test in laboratory. As shown in Fig. 8, four testing magnetometers (S3–S6) are mounted on a test support. S3 and S4 are at the same height with Sensor 1, while S5 and S6 are at the same height with Sensor 2. After the rover get out of place when the test is accomplished, S3 and S5 are used to measure the ambient field (absolute value) of the positions of S1 and S2, respectively. During the rover operation period, S3 and S5 are placed ahead the rover. The distance between S3/S5 and S1/S2 is 30 cm. The test support is vertical to the Rover body. That is to say, the distance between S4/S6 and S1/S2 is $30 \cdot \sqrt{2}$ cm. S7 is used to monitor the time-varying of the ambient field during the rover operation period. In the rover mechanical coordinate frame, z points to the direction of the rover's motion and y points to the right direction of the rover's motion.

Figure 9 gives the RoMAG observations in the rover mechanical coordinate frame. Each payload operation period is listed in Table 5. It is found that there are strong dynamic interferences during the Multispectral Camera operation period for both sensors. Because Sen-

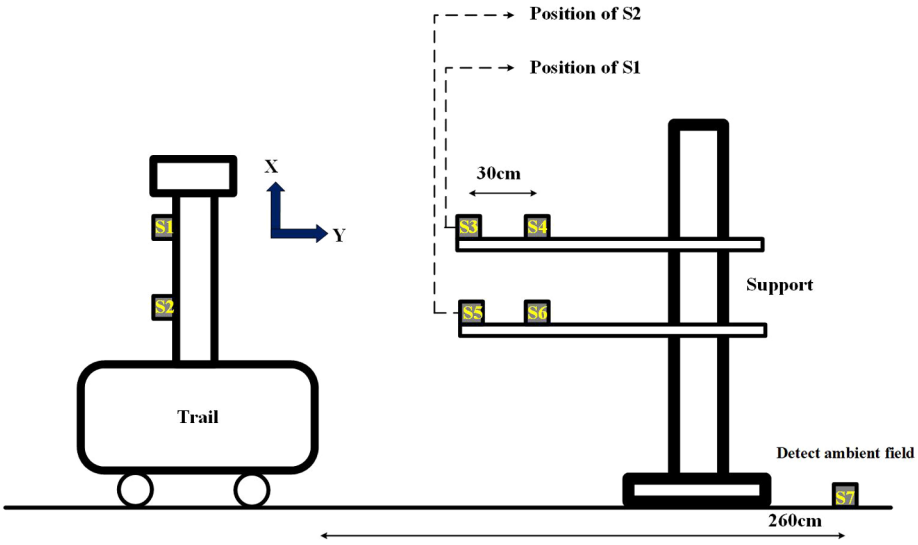

Fig. 8 Prelaunch magnetic test. Four testing magnetometers (S3–S6) are mounted on a test support. S3 and S4 are at the same height with Sensor 1, while S5 and S6 are at the same height with Sensor 2. After the Rover get out of place when the test is accomplished, S3 and S5 are used to measure the ambient field of the positions of S1 and S2, respectively. S7 is used to monitor the time varying of the ambient field during the rover operation period

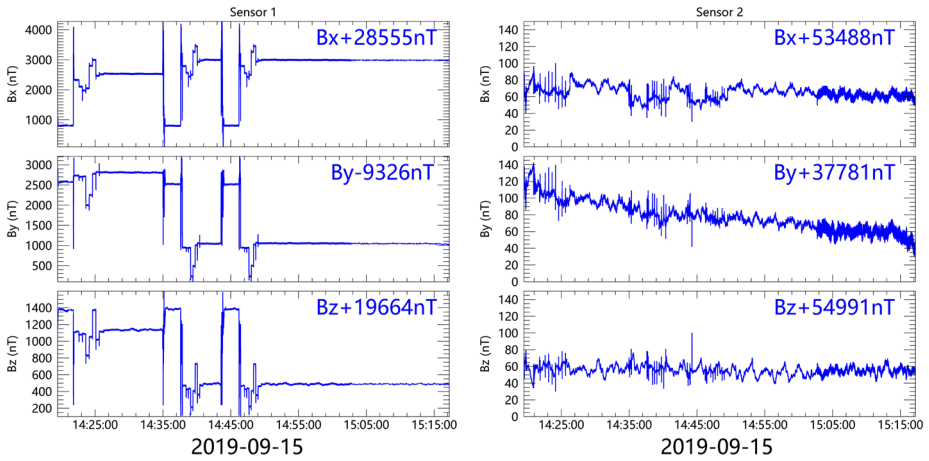

Fig. 9 The RoMAG observations (32 Hz) in the Rover mechanical coordinate

sor 1 is closer to the Camera than Sensor 2, the dynamic interference for sensor 1 is much stronger than that for sensor 2.

Due to different locations, the sensors measure the disturbing sources of the rover in different ways. Therefore, changing rover fields produce different magnetic variations at the locations of the sensors. It would lead to reduction of the relevance between the two-sensor data. In order to investigate the correlation between the magnetic fields at two sensors, we calculate the wavelet spectra of magnetic field components with a period range spanning

Table 5 The payloads operation periods

Payload	Operation period
RoMAG	14:19:29–15:17:12
MSCam	14:19:29–14:26:39 14:35:04–14:41:04 14:43:36–14:49:36
MCS	14:44:29–15:02:59

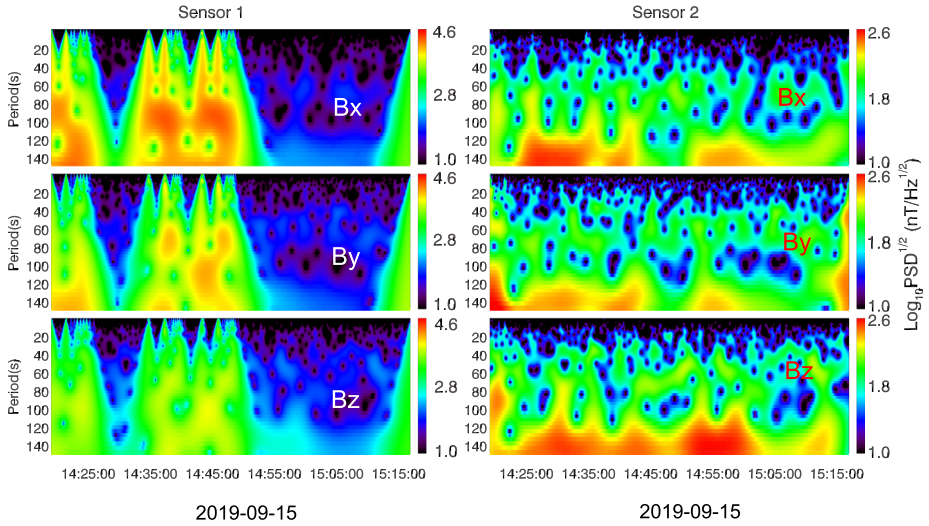

Fig. 10 The wavelet spectra of magnetic field components observed by two sensors

from 16 s to 150 s for two sensors, respectively. As shown in Fig. 10, during the period of MSCam operation, both sensors show strong magnetic fluctuations. The magnetic spectra of sensor 1 shows broadband spectra signature for all the period range while sensor 2 shows strong spectra at about 140 s. The different spectra signature between the two sensors is probably caused by that the short period dynamic interferences at sensor 2 are attenuated because the distance from MSCam to sensor 2 is larger than that of sensor 1. After that period, both sensors show weak magnetic spectra which indicates small interferences from other payloads onboard the rover.

In order to study the dynamic interferences at the two sensors more clearly, we also calculate the wavelet coherence between the sensors pair (Fig. 11). Wavelet coherence spectra are computed by using the complex Morlet wavelet as mother wavelet. As expected, all the three magnetic components have low coherence between the two sensors during the interval 14:19–14:50, which coincide with the operation period of MSCam. This is consistent with the magnetic spectra differences between the sensors pair as shown in Fig. 10. In contrast, during the time interval 14:50–15:17, although the magnetic field of both sensors shows weak oscillation (see Fig. 10), their coherence appears to be high. This indicates the magnetic field at the two sensors exhibit similar oscillation characteristics, which may be mostly the natural magnetic signal signatures.

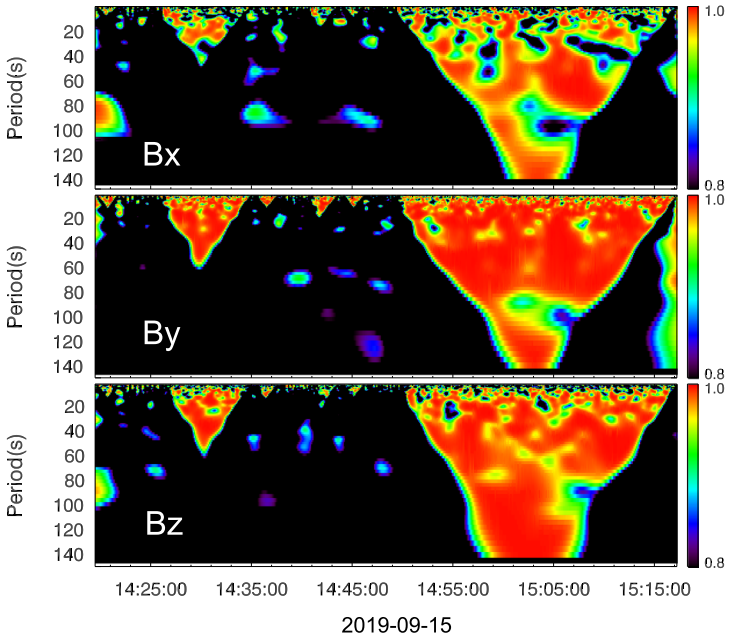

Fig. 11 The wavelet coherence spectra for the sensors pair

To assure the quality of compensated data, we selected the data with high coherence. We use Eq. (2) to determine if the Rover field changes during a time interval dt, as shown in Fig. 12.

$$\Delta \boldsymbol{B}_{\boldsymbol{d}} = |\Delta \boldsymbol{B}_{s1} - \Delta \boldsymbol{B}_{s2}| < e \tag{2}$$

where

$$\Delta \boldsymbol{B}_{s1} = \boldsymbol{B}_{s1}(t+1) - \boldsymbol{B}_{s1}(t)$$

$$\Delta \boldsymbol{B}_{s2} = \boldsymbol{B}_{s2}(t+1) - \boldsymbol{B}_{s2}(t)$$

We set e as 2 nT empirically. If data meet the condition of Eq. (2) and exhibit a duration of at least 10 minutes, it will be selected as high coherence data to be conducted magnetic inference compensation. The select data are indicated by red line in Fig. 12.

The rover-generated fields can be grouped into three types: permanent, induced, and dynamic magnetic fields. The permanent magnetic fields are caused by the permanent magnetism of the ferromagnetic parts of the rover platform. The induced magnetic fields are created in paramagnetic parts by the ambient magnetic field. The dynamic magnetic fields are current-generated field, such as from the power subsystems, solar arrays, batteries, etc. (Acuña et al. 2001).

Applied to both sensors, the magnetic field can be modeled in the payload coordinates

$$\boldsymbol{B}_{\boldsymbol{m}} = \boldsymbol{S} \cdot \boldsymbol{P} \cdot \left[(\boldsymbol{B}_{\boldsymbol{a}} + \boldsymbol{K}_{\boldsymbol{i}} \cdot \boldsymbol{B}_{\boldsymbol{a}} + \boldsymbol{B}_{\boldsymbol{p}} + \boldsymbol{B}_{\boldsymbol{d}}) + \boldsymbol{O} \right] \tag{3}$$

where $\boldsymbol{B}_{\boldsymbol{m}}$ is measured field. $\boldsymbol{B}_{\boldsymbol{a}}$ is ambient field. $\boldsymbol{K}_{\boldsymbol{i}}$ is magnetic induction coefficient as a diagonal matrix. $\boldsymbol{B}_{\boldsymbol{p}}$ is the residual magnetic field. $\boldsymbol{B}_{\boldsymbol{d}}$ is dynamic field, $\boldsymbol{S}$ is a diagonal matrix of scale factors, $\boldsymbol{P}$ is orthogonality matrix, $\boldsymbol{O}$ is offset vector.

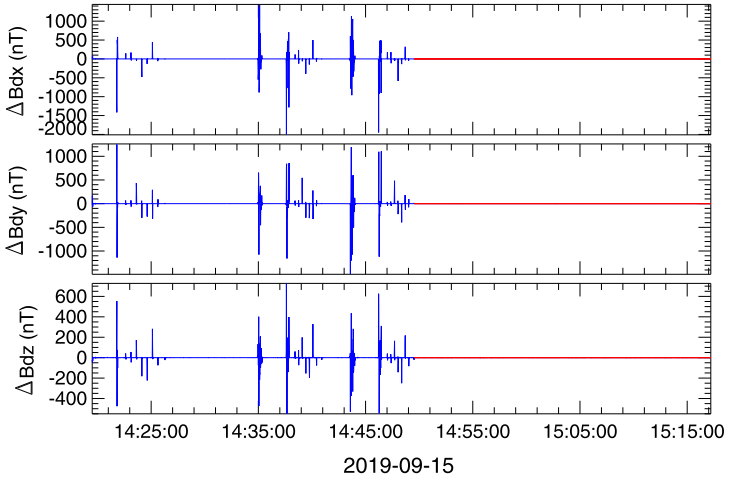

Fig. 12 The Rover field changes during a time interval

Table 6 The magnetic interference parameters

		$\boldsymbol{K_i}$	$\boldsymbol{B_p + B_d}$ (nT)
Sensor 1	X	5.405×10^{-5}	−13816.6
	Y	0.000343	−17247.5
	Z	2.264×10^{-5}	−11344.4
Sensor 2	X	5.300×10^{-5}	13270.9
	Y	0.000267	28880.7
	Z	2.252×10^{-5}	24248.4

Equation (3) can be rewritten as

$$\boldsymbol{B_m} = \boldsymbol{K} \cdot \boldsymbol{B_a} + \boldsymbol{b} \tag{4}$$

where

$$\boldsymbol{K} = \boldsymbol{S} \cdot \boldsymbol{P} + \boldsymbol{S} \cdot \boldsymbol{P} \cdot \boldsymbol{K_i}$$

$$\boldsymbol{b} = \boldsymbol{S} \cdot \boldsymbol{P} \cdot (\boldsymbol{B_p} + \boldsymbol{B_d}) + \boldsymbol{S} \cdot \boldsymbol{P} \cdot \boldsymbol{O}$$

Solve the linear equation (4), we can obtain the $\boldsymbol{K_i}$ and the sum of $\boldsymbol{B_p}$ and $\boldsymbol{B_d}$. Table 6 gives the calculated value of $\boldsymbol{K_i}$ and $\boldsymbol{B_p} + \boldsymbol{B_d}$ at each install position of two sensors in the rover coordinates. Figure 13 gives the comparison of magnetic field measurements data after compensation with ambient field. The RMS errors of compensation algorithm for three components are all less than 1.5 nT.

However, there are many additional disturbances to be further taken into account. For example, due to some engineering factors, the solar arrays were not installed on the rover and MarSCoDe wasn't in operation in the preflight magnetic test. Therefore, the disturbances generated by these sources should be carefully checked, identified, and eliminated in future.

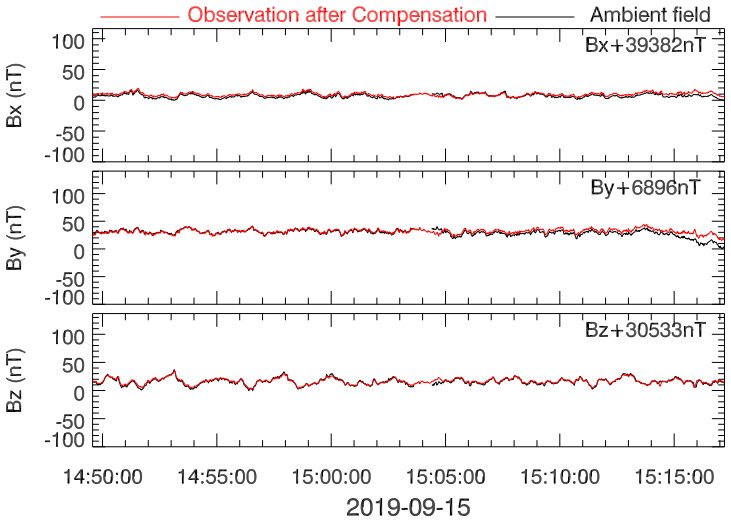

Fig. 13 A comparison of magnetic field measurements data after compensation with ambient field. Red: data after correction (1 Hz), black: ambient field

4 Summary

The RoMAG will provide the first mobile vector magnetic field observations at sample rates of up to 32 Hz and obtain fine-scale structure of crust field. Two magnetometers are installed on the top and bottom of the mast of Rover, respectively. Due to the fact that RoMAG is placed in the vicinity of micro-motors, the magnetic interference compensation technique is developed to remove the magnetic field disturbances. However, the disturbances generated by the solar arrays and surface composition instruments operation should be carefully identified and eliminated during in-flight calibration processing. Together with the magnetic field observations by the magnetometer on the obiter of TianWen-1, the RoMAG observation data will help us to understand Martian internal structure, space electromagnetic environment, and the evolutionary history of atmosphere and climate.

Acknowledgements This work is supported by the Strategic Priority Research Program of Chinese Academy of Sciences (Grant No. XDB41010304), Beijing Municipal Science and Technology Commission (Grant No. Z191100004319001), the pre-research Project on Civil Aerospace Technologies No. D020103 funded by CNSA, and the National Natural Science Foundation of China (41874080, 41674168, 41874197).

References

M.H. Acuña, J.E.P. Connerney, P. Wasilewski et al., Magnetic field and plasma observations at Mars: initial results of the Mars Global Surveyor mission. Science **279**, 1676–1680 (1998)

M.H. Acuña, J.E.P. Connerney, N.F. Ness et al., Global distribution of crustal magnetism discovered by the Mars Global Surveyor MAG/ER experiment. Science **284**, 790–793 (1999)

M.H. Acuña, J.E.P. Connerney, P. Wasilewski et al., The magnetic field of Mars: summary of results from the aerobraking and mapping orbits. J. Geophys. Res. **106**, 23403–23417 (2001)

H.-U. Auster, I. Apathy, G. Berghofer, A. Remizov, R. Roll, K.-H. Fornaçon, K.H. Glassmeier, G. Haerendel, I. Hejja, E. Kührt, W. Magnes, D. Moehlmann, U. Motschmann, I. Richter, H. Rosenbauer, C.T. Russell, J. Rustenbach, K. Sauer, K. Schwingenschuh, I. Szemerey, R. Waesch, ROMAP: Rosetta magnetometer and plasma monitor. Space Sci. Rev. **128**(1–4), 221–240 (2007). https://doi.org/10.1007/s11214-006-9033-x

H.-U. Auster, K.H. Glassmeier, W. Magnes, O. Aydogar, W. Baumjohann, D. Constantinescu, D. Fischer, K.-H. Fornaçon, E. Georgescu, P. Harvey, O. Hillenmaier, R. Kroth, M. Ludlam, Y. Narita, R. Nakamura, K. Okrafka, F. Plaschke, I. Richter, H. Schwarzl, B. Stoll, A. Valavanoglou, M. Wiedemann, The THEMIS fluxgate magnetometer. Space Sci. Rev. **141**(1–4), 235–264 (2008). https://doi.org/10.1007/s11214-008-9365-9

D. Banfield, J.A. Rodriguez-Manfredi, C.T. Russell et al., InSight Auxiliary Payload Sensor Suite (APSS). Space Sci. Rev. **215**, 4 (2019)

J.E.P. Connerney, M.H. Acuña, N.F. Ness, G. Kletetschka, D.L. Mitchell, R.P. Lin, H. Reme, Tectonic implications of Mars crustal magnetism. Proc. Natl. Acad. Sci. **102**, 14970–14975 (2005)

J.E.P. Connerney, J. Espley, P. Lawton, S. Murphy, J. Odom, R. Oliversen, D. Sheppard, The MAVEN magnetic field investigation. Space Sci. Rev. **195**, 257–291 (2015)

S.S. Dolginov, Y.G. Yeroshenko, L.N. Zhuzgov, Magnetic field in the very close neighborhood of Mars according to data from the Mars 2 and Mars 3 spacecraft. J. Geophys. Res. **78**, 4779–4786 (1973)

S.S. Dolginov, Y.G. Yeroshenko, L.N. Zhuzgov, The magnetic field of Mars according to the data from the Mars 3 and Mars 5. J. Geophys. Res. **81**, 3353–3362 (1976)

K.-H. Glassmeier, H.-U. Auster, D. Heyner, K. Okrafka, C. Carr, G. Berghofer, B.J. Anderson, A. Balogh, W. Baumjohann, P. Cargill, U. Christensen, M. Delva, M. Dougherty, K.-H. Fornaçon, T.S. Horbury, E.A. Lucek, W. Magnes, M. Mandea, A. Matsuoka, M. Matsushima, U. Motschmann, R. Nakamura, Y. Narita, H. O'Brien, I. Richter, K. Schwingenschuh, H. Shibuya, J.A. Slavin, C. Sotin, B. Stoll, H. Tsunakawa, S. Vennerstrom, J. Vogt, T. Zhang, The fluxgate magnetometer of the BepiColombo Mercury Planetary Orbiter. Planet. Space Sci. **58**, 287–299 (2010)

D. Herčík, H.U. Auster, J. Blum, K.H. Fornaçon, M. Fujimoto, K. Gebauer, C. Güttler, O. Hillenmaier, A. Hördt, E. Liebert, A. Matsuoka, R. Nomura, I. Richter, B. Stoll, B.P. Weiss, K.H. Glassmeier, The MASCOT magnetometer. Space Sci. Rev. (2016). https://doi.org/10.1007/s11214-016-0236-5

C.L. Johnson, A. Mittelholz, B. Langlais, C.T. Russell, V. Ansan, D. Banfield, P.J. Chi, M.O. Fillingim, F. Forget, H.F. Haviland, M. Golombek, S. Joy, P. Lognonné, X. Liu, C. Michaut, L. Pan, C. Quantin-Nataf, A. Spiga, S. Stanley, S.N. Thorne, M.A. Wieczorek, Y. Yu, S.E. Smrekar, W.B. Banerdt, Crustal and time-varying magnetic fields at the InSight landing site on Mars. Nat. Geosci. (2020). https://doi.org/10.1038/s41561-020-0537-x

N. Olsen, L. Tøffner-Clausen, T.J. Sabaka, P. Brauer, J.M.G. Merayo, J.L. Jørgensen, J.-M. Léger, O.V. Nielsen, F. Primdahl, T. Risbo, Calibration of the Ørsted vector magnetometer. Earth Planets Space **55**, 11–18 (2003)

W. Riedler, D. Möhlmannt, V.N. Oraevsky, K. Schwingenschuh, Ye. Yeroshenko, J. Rustenbacht, Oe. Aydogar, G. Berghofer, H. Lichtenegger, M. Delva, G. Schelch, K. Pirsch, G. Fremuth, M. Steller, H. Arnold, T. Raditsch, U. Austert, K.-H. Fornacont, H.J. Schenkt, H. Michaelist, U. Motschmann, T. Roatscht, K. Sauer, R. Schrotert, J. Kurths, D. Lenners, J. Linthe, V. Kobzev, V. Styashkin, J. Achachell, J. Slavin, J.G. Luhmann, C.T. Russell, Magnetic fields near Mars: first results. Nature **341**, 604–607 (1989)

E.J. Smith, L. Davis Jr., P.J. Coleman Jr., D.E. Jones, Magnetic field measurements near Mars. Science **149**, 1241–1242 (1965)

T.L. Zhang, W. Baumjohann, M. Delva, H.-U. Auster, A. Balogh, C.T. Russell, S. Barabash, M. Balikhin, G. Berghofer, H.K. Biernat, H. Lammer, H. Lichtenegger, W. Magnes, R. Nakamura, T. Penz, K. Schwingenschuh, Z. Vörös, W. Zambelli, K.H. Fornacon, K.-H. Glassmeier, I. Richter, C. Carr, K. Kudela, J.K. Shi, H. Zhao, U. Motschmann, J.-P. Lebreton, Magnetic field investigation of the Venus plasma environment: expected new results from Venus Express. Planet. Space Sci. **54**, 1336–1343 (2006)